ON THE BOUNDARY CONDITIONS AND SPATIAL STRUCTURE OF TURBULENT JET FLAMES OF DILUTE SPRAYS

A. R. Masri*, J. Gounder, W. O'Loughlin* and L. DeFina***
assaad.masri@sydney.edu.au
*School of Aerospace, Mechanical and Mechatronic Engineering,
The University of Sydney, NSW 2006 Australia
**Duetsches Zentrum Für Luft und Raumfahrt, Institut für Verbrennungstechnik
70569 Stuttgart Germany

Abstract
This paper discusses the spatial structure of reaction zones in turbulent flames of dilute sprays of methanol and ethanol fuels. Additionally, the paper highlights the importance of specifying the boundary conditions in experimental jets of dilute sprays. Measurements of axial velocity fields at the jet exit plane show bimodal distributions for large droplets near the inner wall of sufficiently long tubes. High speed images of Mie scattering from droplets reveal that such bimodality is due to droplet shedding from the boundary layer that develops on the inner wall of the pipe. This paper also reports images Laser induced fluorescence (LIF) of OH and acetone in flames of acetone sprays as well as images of LIF-OH and formaldehyde in flames of ethanol sprays. The information reveals an interesting evolution of the reaction zones changing from thin to thick regions depending on the level of partial premixing that takes place. The paper discusses the effects of increasing the jet velocity or the spray loading on the structure of the reaction zones.

Introduction
Advancing current capabilities to compute the structure of spray flames requires the correct representation of many physical sub-processes such as primary and secondary atomization, coalescence and dispersion, droplet evaporation and interaction with the surrounding turbulence and heat release, as well as droplet combustion [1-11]. With dilute sprays, which are the subject of this paper, the latter two processes are more dominant and the question of how reaction zones evolve within the droplet fields becomes one of prime importance [11-16]. Whether combustion occurs around single droplets or droplets clouds depends on many factors related to the properties of the fuel as well as the local flow conditions. The Group Combustion number is one parameter devised to characterize such demarcation [17-20]. It should also be noted that the local flame structure is directly affected by the stratification or partial premixing which in turn is controlled by the physical properties of the evaporating droplets as well as the local turbulence.

Another key issue that controls the accuracy of calculating the structure of spray flows is the adoption of correct boundary conditions. This is an essential requirement for model burners in general if these are to be useful as benchmarks for the development of physical sub-models and the validation of computational approaches. The relevance of this condition has been clearly demonstrated and emphasized in the burners employed by the turbulent non-premixed workshops on measurements and computations of turbulent non-premixed flames (TNF) [21, 22]. With spray burners, satisfying the requirement of well-known boundary conditions is more complex than in gaseous flows. Injecting sprays directly into the flow, while more convenient is clearly not preferred by modelers due to uncertainties in representing the droplet fluxes and size distributions. Forming the spray early and guiding it into the experiment

provides better control of these parameters at the initial condition of the experiment. However, this mode of injection causes some concern [23, 24] particularly if the droplets are guided through a pipe as is the case with the burner studied here.

This paper sheds light on both issues discussed above, namely combustion of dilute sprays and the related boundary conditions. Planar imaging of selected scalars using Laser Induced Fluorescence (LIF) is applied to a range of dilute spray flames of acetone and ethanol fuels. The imaged scalars, albeit qualitative, are assumed to be indicative of the spatial structure of the reaction zones and these are presented under different conditions of changing carrier velocity and spray loading. A feature of this burner is that the spray is formed upstream and is carried to the exit plane of the pipe using a co-flowing stream of air (or nitrogen). The interaction of the droplets with the pipe during transit causes an issue at the exit plane near the pipe wall where the measured velocity of larger droplets tends to be bimodal and hence, resulting in apparent high rms fluctuations. This anomaly is further scrutinized in this paper using a variety of pipe lengths and diameters to guide the spray-air mixture.

Experimental

Burner and flames:

Full details of the piloted spray burner can be found elsewhere [24] and only a brief description is given here. Spray is generated using a Sono-Tek ultrasonic nebulizer located 215 mm upstream and is advected to the burner's exit plane with a co-flowing stream of carrier air. The central fuel tube, with an inner diameter of 10.5 mm is surrounded by an annular pilot flame holder, which is 25mm in diameter and has 72 holes concentrically aligned at 7.0 mm, 9.0 mm and 11 mm from the centre. Each row contains 24 holes with diameters 0.9 mm, 1.0 mm and 1.1 mm respectively. A co-flow of diameter 104 mm surrounds the burner and the co-flow/burner assembly is mounted in a vertical wind tunnel. The tunnel exit has a cross section of 290 x 290 mm. The exit plane of the co-flow and nozzle are located 59.0 mm downstream of the exit plane of the wind tunnel. The co-flowing air velocity is fixed at 4.5 m/s, and the pilot unburnt velocity is fixed at 1.5 m/s with an equivalence ratio of 1.0 so that the main controlling parameters for the flames are the mass flow rates of liquid fuel and the bulk velocity of the carrier fluid.

For each of the acetone and ethanol fuels (referred to as AcF and EtF, respectively), six cases are chosen to study the effects of increasing the carrier velocity at a fixed liquid flow rate (referred to as sequence 1, 2, 5 and 7) or the effects of increasing the liquid fuel flow rate for a fixed carrier velocity (referred to as sequence 4, 3, and 1). To facilitate comparison, cases with the same numerical reference (such as AcF1 and EtF1) have similar mass flow rates for both carrier gas and liquid fuel. Three liquid fuel mass flow rates are used, namely 23.4, 45 and 75 g/min and these are referred as "Low", "Mid" and "High" respectively. Also, four carrier velocities of 24, 36, 48 and 60 m/s (corresponding respectively to carrier mass flow rates of 150, 225, 301 and 376 g/min) are employed as shown in Tables 1 and 2. It should be noted that air has been used as carrier for all the cases studied in this paper.

Joint LIF-OH-acetone is performed in acetone flames. The $Q_1(6)$ line of the (0,1) vibrational band of the $X\ ^2\Pi$-$A^2\Sigma^+$ transition at 283.9 nm is used as a single laser source to simultaneously excite LIF-OH and acetone. The laser pulse energy was measured to be 4 mJ and the laser beam was focused into a 150 micron thick sheet using a 300 mm focal length cylindrical lens. Joint LIF-OH-CH_2O and Mie scattering was imaged in ethanol flames. The set-up for LIF-OH remains unchanged as described above for acetone. Formaldehyde (CH_2O) was excited in 4^1_0 vibrational transition in the $\tilde{A}^1A_2$-$\tilde{X}^1A_1$ band near 353.17 nm and this same

line was used to collect Mie scattering from ethanol droplets at 353.17 nm. LIF-OH-acetone and LIF-OH-CH_2O was collected on two intensified Flowmaster CCD cameras located on opposite sides of the flame. The LIF-OH signal is filtered using a high pass WG-295 filter and an interference filter centred at 310 nm with a 10 nm bandwidth while broadband LIF-acetone is filtered using a Schott glass filter GG-400 and low pass filter SPF-450. The broadband LIF-CH_2O signal is filtered using a Schott glass filter GG-400 and low pass filter SPF-450. The droplet Mie signal is not intensified and passes through an interference filter centred at 355 nm with a bandwidth of 10 nm.

Table 1 Initial conditions for the acetone flames.

Reacting Spray Cases - Acetone	**AcF 1**	**AcF 2**	**AcF 3**	**AcF 4**	**AcF 5**	**AcF 7**
Bulk Jet Velocity U_{jet} (m/s)	24	36	24	24	48	60
Carrier mass flow rate (g/min)	150	225	150	150	301	376
Liquid fuel injection rate (g/min)	75	75	45	23.4	75	75
Measured liquid flow at exit (g/min)	18.0	23.9	15.9	7.2	27.8	31.1
Vapor fuel flow at jet exit (g/min)	57.0	51.1	29.1	16.2	47.2	43.9
Overall equivalence ratio, $\Phi_{overall}$	4.7	3.2	2.9	1.5	2.4	1.9
Equivalence ratio at jet exit, Φ_{exit}	3.6	2.2	1.8	1.0	1.5	1.1

Table 2 Initial conditions for the ethanol flames.

Reacting Spray Cases - Ethanol	**EtF 1**	**EtF 2**	**EtF 3**	**EtF 4**	**EtF 5**	**EtF 7**
Bulk Jet Velocity U_{jet} (m/s)	24	36	24	24	48	60
Carrier mass flow rate (g/min)	150	225	150	150	301	376
Liquid fuel injection rate (g/min)	75	75	45	23.4	75	75
Measured liquid flow at exit (g/min)	45.7	66.6	30.7	14.5	70.1	73.0
Vapor fuel flow at jet exit (g/min)	29.3	8.4	14.3	8.9	4.9	2.0
Overall equivalence ratio, $\Phi_{overall}$	4.7	3.2	2.9	1.5	2.4	1.9
Equivalence ratio at jet exit, Φ_{exit}	1.75	0.34	0.85	0.53	0.15	0.05

While it is known that interference from PAH molecules affects LIF-CH_2O particularly in fuel rich conditions, the question here is whether such effects are significant in the regions of heat release so that the product CH_2OxOH is corrupted by PAH. Simple laminar flame calculations using a detailed mechanism that includes some PAH species confirm that there is no overlap between the mass fraction profiles of the representative PAH molecules and the rate of heat release represented by the product of CH_2OxOH. Hence, even though PAH interferes with CH_2O in rich mixtures ($\xi > 0.1$), the region where heat release is significant as marked by CH_2OxOH, is generally free from such interferences.

Non-reacting studies of pipe effects:

In order to study the effects of the fuel pipe guiding the spray to the burner's tip, six different pipe configurations are investigated using non-reacting sprays of mineral turpentine. Three configurations use the pipe length of 196 mm (which is adopted for the reacting cases) but with decreasing inner diameters of 10.1 mm, 7 mm and 3.5 mm and three other configurations for the 10.1mm diameter tube but with decreasing length of 196 mm, 96 mm and 6 mm. Two

different carrier velocities are tested, namely 24 m/s and 60 m/s as well as various different levels of fuel loading. Table 3 shows details of the conditions studied.

The position of the ultrasonic spray atomizer with respect to the tube inlet is unchanged throughout these tests. The atomizer is designed to produce a droplet distribution with a Sauter mean diameter of approximately 40 μm when used with water although this may vary with the specific fuel used. The nebuliser produces droplets that have a near zero initial momentum such that the velocity of the droplets at the exit plane of the tube is dictated entirely by the carrier velocity. Measurements of velocity across the exit plane of each configuration were performed using the standard LDV/PDA method.

Table 3: Flow conditions for the various cases and pipe lengths studied.

	Case A			**Case B**			**Case C**		
Tube Diameter (mm)	10.1	7.0	3.5	10.1	7.0	3.5	10.1	7.0	3.5
Carrier air velocity (m/s)	24	24	24	24	24	24	60	60	60
Carrier air Reynolds number (Re_A)	15 700	10900	5400	15 700	10900	5400	39 300	27200	13600
Carrier mass flow rate (g/min)	138.8	66.7	16.7	138.8	66.7	16.7	347.9	167.1	41.8
Mass ratio of fuel/air flow	0.16	0.16	0.16	0.50	0.50	0.50	0.20	0.20	0.20
Fuel injection rate (g/min)	21.7	10.4	2.6	69.4	33.3	8.3	69.4	33.3	8.3

High speed imaging (5kHz) of Mie scattering from droplets was performed at the exit plane of the six pipes studied here using a dual head Edgewave, Nd:YAG diode pumped laser. The second harmonic output of the laser (532 nm) is formed into a vertical sheet of height 13 mm and the two heads are configured to produce two separate overlapping beams (overlapped in space but not time) that are passed over the exit plane through the centerline of the spray tube. The time interval between the beams is set at 30 μs. A high speed CMOS camera (HSS6) run in double frame mode coupled with a Komura 85mm, F#1.4 lens is used to capture the Mie scattering from the droplets. A filter with a FWHM of 10 nm and centered at 532 nm is used to filter out unwanted signals.

Results and Discussion

Flame structure:

Figure 1 shows samples of representative simultaneous LIF-OH-acetone images measured at various axial stations in the five acetone flames listed in Table 1. The measurements are presented here at upstream locations of x/D=5, 10 and 15, where x is the axial distance and D is the spray jet diameter. The trends shown by flames AcF4, AcF3 and AcF1 represent the effects of increasing fuel flow rate (at a fixed air carrier velocity) while the trends shown by flames AcF1, AcF5 and AcF7 represent the effects of increasing carrier velocity (at a fixed fuel loading). The top and middle frames of each image set represent LIF-OH and LIF-acetone respectively and the third frame contains the superimposed image of LIF-acetone-OH. The individual frame size is 29x15 mm. On the intensity color scale, black represents 0 and red maximum intensity, while white represents a saturated signal. LIF-acetone was collected on a intensified camera setup in order to obtain a high signal to noise ratio from the

vapor and thus LIF intensity from the large liquid acetone droplets are saturated and are marked by white spots on the LIF image. The droplet size on the images is considerably larger than the actual droplet and this is due to intensifier blooming effect. Close to the jet exit plane, all the fuel is confined to the center of the jet and is shrouded by the pilot flame. Large amounts of fuel evaporates inside the burner and as the fuel loading increases the amount of acetone vapor also increases creating a non-combustible rich mixture of fuel and air exiting the nozzle. This is confirmed by the large values of Φ_{exit} reported for these flames in Table 1.

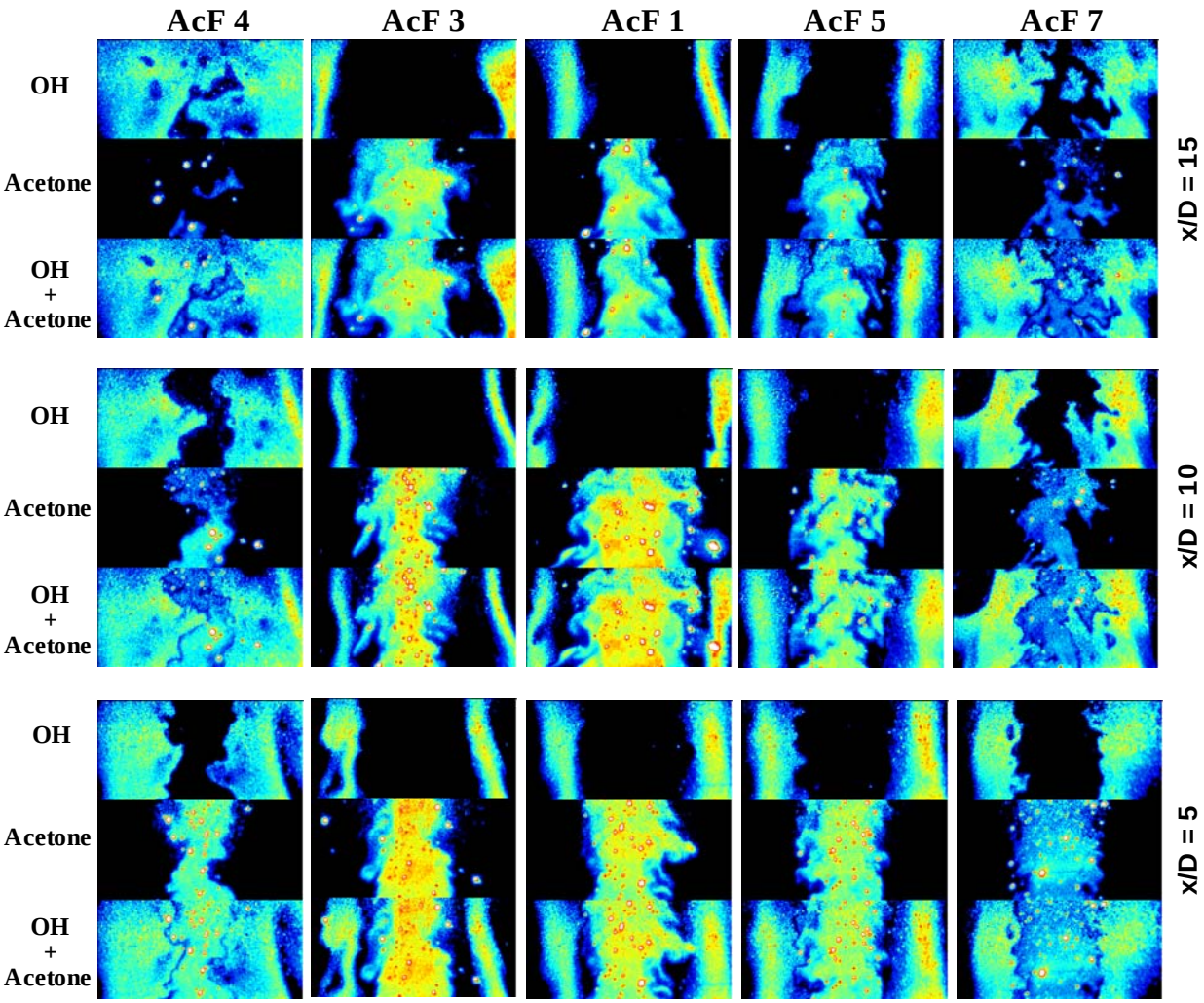

Figure 1: Simultaneous and instantaneous LIF images of OH, acetone and acetone/OH image combined together (OH+Acetone) measured at x/D=5, 10 and 15 in flames AcF4, AcF3, AcF1 AcF5 and AcF7.

At x/D=5, flame AcF4 shows broad OH fields wrapping around the outer edges of the acetone fuel almost without any separation. This is different from flames AcF3 and AcF1 which show thin smooth OH zones with clear separation between the fuel and the reaction zone (marked tentatively by the presence of OH). It is worth noting that increasing the carrier velocity in flames AcF5 and AcF7 reduces this separation again such that the structure for flames AcF4 and AcF7 are similar. Further downstream at x/D=10, the concentration of liquid acetone in the centre of the jet reduces significantly from flames AcF4 and AcF7 while the OH zones are even broader which is more akin to premixed flames rather than non-premixed particularly at such upstream locations. Interestingly, flames AcF3 and AcF1 show a totally opposite trend

where the fuel zones are even wider and the OH fields are thinner and pushed further away from the jet centerline as expected for diffusion flames. At x/D = 15, the OH fields cover the entire image for flames AcF4 and AcF7 with scattered patches of OH even on the centerline wrapping around pockets of cold unreacted fuel that may contain droplets of acetone. Flames AcF3 and AcF1 exhibit very little change in the overall structure at this location and show, along with flame AcF5, thin OH zones surrounding a wide field of rich mixture of fuel and carrier air in the center of the jet.

The pattern observed in Fig. 1 for acetone flames is interesting and can be summarized as follows: at sufficiently low liquid fuel loading and carrier air velocity (AcF4), the gas emerging from the jet exit plane appears to be sufficiently premixed to form broad OH profiles and hence broad reaction zones surrounding the central fuel core which reduces in concentration further downstream leading to further broadening in the reaction zones. As the liquid fuel loading increases for the same carrier velocity (AcF3 and AcF1), a diffusion flame structure is gradually resumed with relatively thin outer reaction zones clearly separated from the central spray core. This structure persists from x/D=5 to 15. With increasing the carrier velocity for the same fuel loading (as for AcF1, AcF5 and AcF7) the trend is reversed and a structure not unlike that of AcF4 is observed for flame AcF7 with AcF5 being a transitional flame from diffusion to premixed-like. It is worth noting that this picture is consistent with the values reported in Table 1 for Φ_{exit} where the richest mixture at the jet exit plane is obtained for flame AcF1 which takes a diffusion-like structure.

Representative, simultaneous LIF images of OH, formaldehyde (CH_2O), droplet Mie scattering and heat release, HR as determined by the product (LIF-OH x LIF-CH_2O) are presented in Fig. 2 for three axial locations in the five ethanol flames listed in Table 2. The trends shown by flames EtF4, EtF3 and EtF1 represent the effects of increasing fuel flow rate (at a fixed air carrier velocity) while the trends shown by flames EtF1, EtF5 and EtF7 represent the effects of increasing carrier velocity (at a fixed fuel loading). The physical size of the individual image is 34x14 mm. The bottom image of each set (labeled HR+Droplet) shows the droplet positions with respect to heat release regions by superimposing the HR image on that of droplets (Mie scattering). The HR+Droplet images were regenerated, for clarity, to have only three color codes where yellow marks the HR region, pale blue marks the droplets and red marks the regions of overlap between HR and droplets. Mie scattering signal from liquid droplets are saturated in order to show small as well as large droplets. Some of the droplets are artificially large due to intensifier blooming effect. The spatial resolution of the droplet image is 25 microns so droplets smaller than 25μm are not resolved.

At x/D=5, flame EtF4 shows a relatively broad reaction zone as represented by the OH image which surrounds the LIF-CH_2O image. The heat release zone lies on the inner edge of this OH region as indicated by the images of HR which in turn surround the inner droplet as shown in the image of HR+Droplet. Increasing the droplet loading for the same carrier velocity (EtF3 and EtF1 leads to the appearance of pockets of OH on the centerline of the jet and these are separated from the outer OH profile which becomes thinner and diffusion like in flame EtF1. This double reaction zone structure is confirmed in the images of HR for flame EtF1 at x/D=5. It is also interesting that the HR+Droplet images show some overlap between HR and the droplets which is not simple to interpret. One possible explanation is that droplets are much smaller than the width of the imaging laser sheets and hence become partly embedded within. Increasing the carrier velocity for the same droplet loading (cases EtF1, EtF5, EtF7) causes the otherwise double reaction zones to mesh together as seen at x/D=5 in flame EtF5.

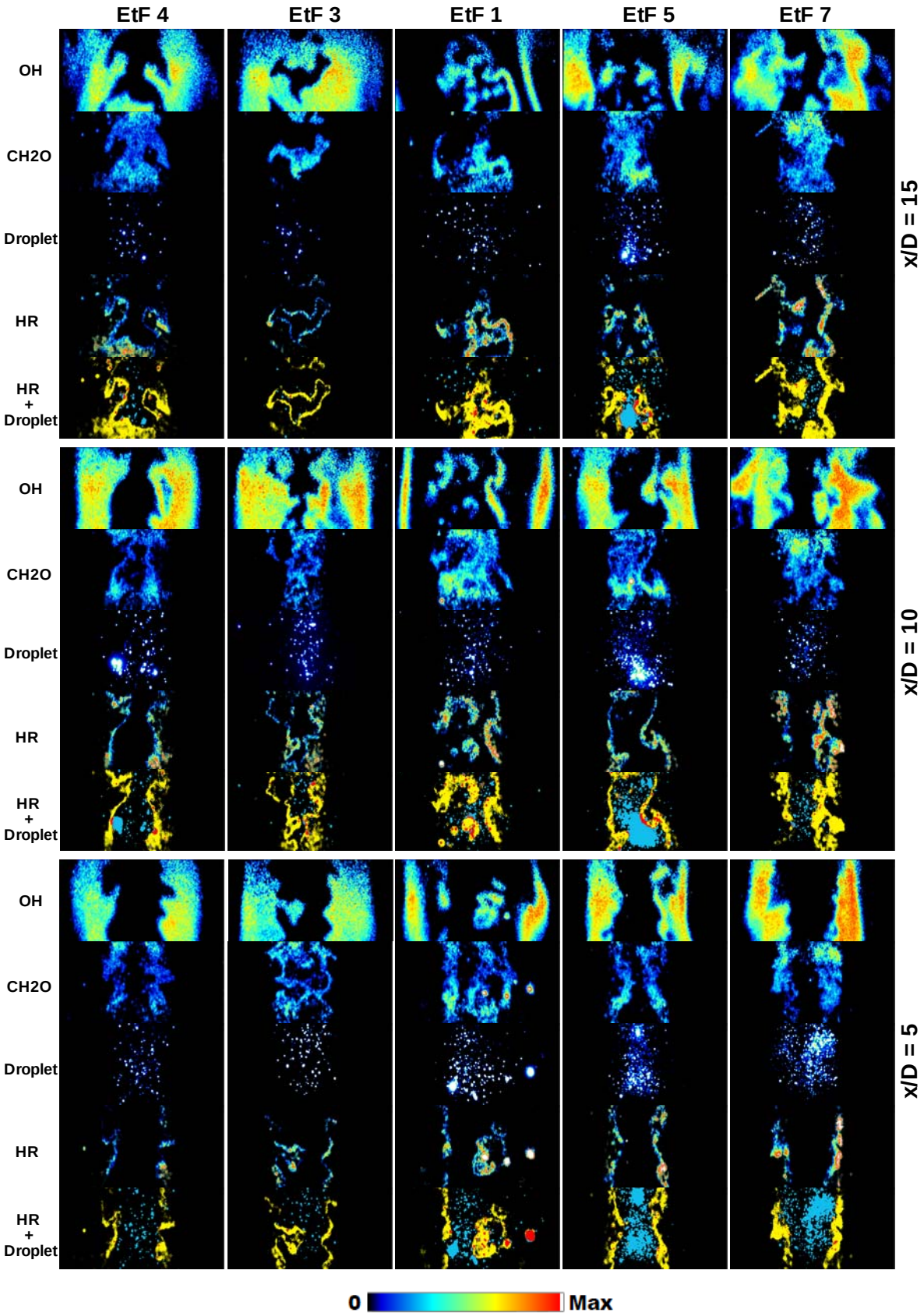

Figure 2: Simultaneous images of LIF OH, LIF CH2O, droplet Mie scattering Droplet), heat release (HR=OH x CH2O) and superimposed image of HR onto droplet image (HR+Droplet) collected at x/D=5, 10 and 15 in flames EtF4, EtF3, EtF1, EtF5 and EtF7.

This is further confirmed in flame EtF7 where a single, broad layer for heat release is obtained at all axial locations. The similarities between the structure of flames EtF4 and EtF7 are also noted here.

Further downstream at x/D=10, the transition from a single broad region in flame EtF4 to a double reaction structure in flames EtF3 and EtF1 is now much clearer as reflected both in the OH as well as the HR images. Flame EtF1 shows thinner OH zones than those of flames EtF4 and EtF3. Increasing the carrier air velocity for the same liquid loading as flame EtF1 (EtF5 and EtF7) broadens and contorts the OH profiles and the double reaction zones are brought closer together but not fully merged even in flame EtF7. It is not until x/D=15 that these double reaction zones merge for flame EtF7 but not EtF5. It is also interesting that the transition from single broad OH profiles to a double reaction zone occurs also at x/D=15 as the liquid fuel loading increases from flame EtF3 to EtF1.

Evaporation of ethanol droplets inside the burner in not as significant as acetone, this is evident from the values of Φ_{exit} shown in Table 2. The equivalence ratio at the jet exit plane increases as the fuel loading is increased to a maximum of 1.75 for EtF1 and then decreases with increasing carrier air velocity. Locally flammable mixtures may be formed at the jet exit plane of flame EtF1 and this is evident from the double reaction structure imaged here. Conversely, flames EtF4 and EtF7 have values of Φ_{exit} that are lean on average and hence double reactions in these flames are not expected. In most flames, the regions of heat release form on the periphery of the fuel vapor/droplet cloud but there are also instances where broad HR regions form in the center of the jet. The latter feature is more common in the lower velocity flames EtF1 and EtF3.

Effects of pipe on spray pattern at exit plane:

Earlier measurements of axial velocity conditioned with droplet size [24] have shown that at the exit plane of the jet, close to the pipe wall, the rms fluctuations of large droplets ($30<d<40$microns) are higher than those of small droplets (less than 10 microns). This aspect is further studied here by providing measurements of velocity at the exit plane of tubes of different diameter and different length (different distances from the spray injection point). Additionally, high speed images of Mie scattering from droplets at the exit plane of selected pipes are also presented.

Figure 3 shows scatter plots of axial velocity versus droplet diameter measured at the jet exit and near the wall of pipes of various lengths and diameters. Also shown next to each scatter plot is a histogram of the axial velocity for a small range of droplet diameters located within the vertical dashed lines shown on the adjacent scatter plots. Plots on the LHS correspond to the large pipe diameter of 10.1 mm while those on the RHS correspond to a narrower tube of 7 mm in diameter. The top row of scatter plots and histograms are taken at the exit plane of the 196 mm long tube while the middle and lower rows correspond to shorter tubes of 96 mm and 6 mm, respectively (note that the middle illustration shows distances along a single pipe but physically refers to pipes of different lengths and diameters). The results shown in Fig. 3 correspond to Case B (shown in Table 3) which has the highest mass ratio of liquid fuel to carrier air.

It is evident from both the scatter plots and the histograms shown in Fig. 3 that the measured velocities near the walls of both the 7 mm and the 10.1 mm diameter tubes exhibit significant scatter over the entire range of droplet diameters. For the long tubes (96 mm and 196 mm), the scatter is extreme and the distributions are bimodal for larger droplet diameters. This

bimodality is clearly seen in the histograms and it explains the high rms fluctuations measured at these locations. For the shorter tube of 6 mm (and up to a length of 30 mm but not shown), the bimodality is lost and the distributions are uniform.

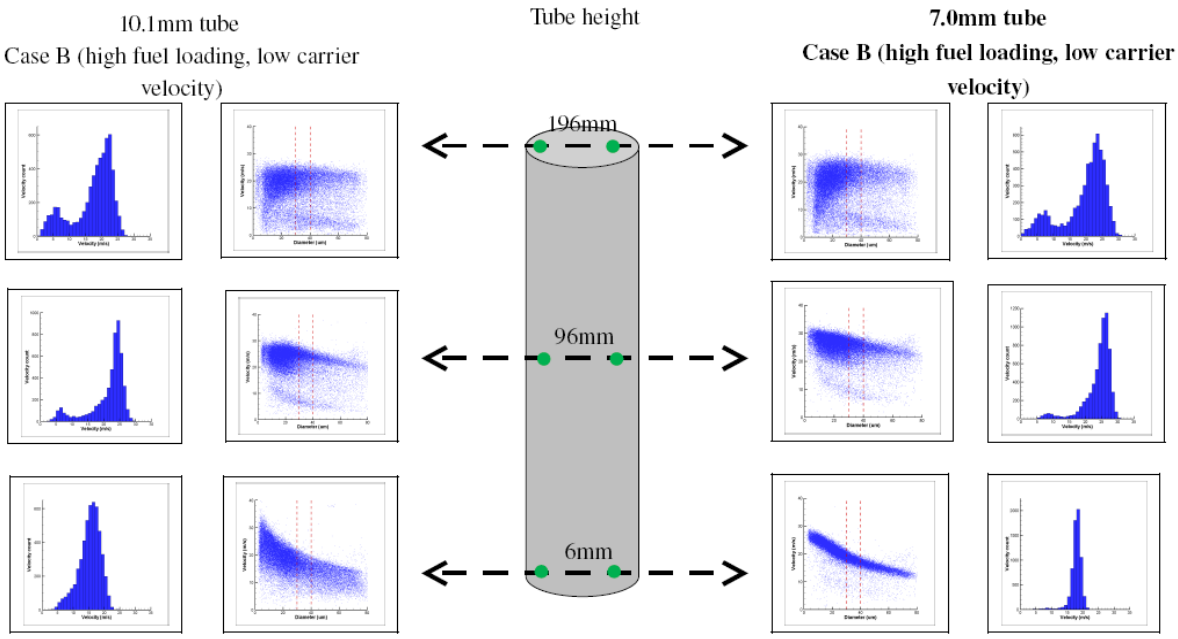

Figure 3: Effect of tube length on bimodality of the spray at the exit plane. Diameter histograms and diameter-velocity plots are shown for three different pipe lengths and two different tube diameters (10.1 mm and 7.0 mm).

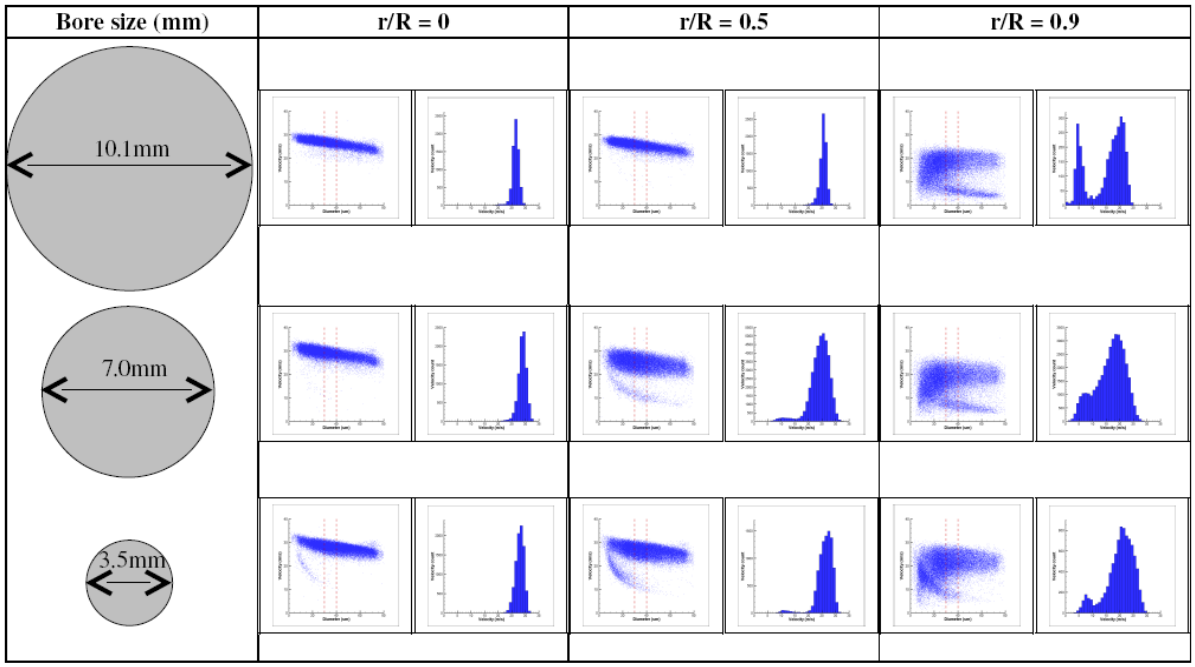

Figure 4: Effect of tube diameter on bimodality of the spray at the exit plane. Diameter histograms and diameter-velocity plots are shown for three different pipe diameters at three different radial locations on the exit plane.

It is believed that the cause of the bi-modality is a result of interactions between the spray and the tube wall. As liquid builds up on the wall it is eventually shed off the wall hence producing large, relatively slow moving droplets that contribute to the lower leg of the bimodal distribution. As the tube length is reduced, less of the spray has had a chance to impact the wall of the jet. For this reason, the amount of droplet shedding from the wall of the jet is reduced and therefore the bimodal nature of the spray is decreased. The 6 mm tube is so short that the spray is completely confined to the region near the center of the jet while the wall is completely dry. This explains the mono-modal velocity distribution close to the wall of the 6mm tube.

Figure 4 shows the effects of changing the tube diameter on the mode of the spray at the exit plane. Scatter plots of the measured axial velocity as well as histograms for the data restricted to within the vertical bars on the scatter plots are shown for three tube diameters at three radial locations on the jet exit plane, namely r/R=0, r/R=0.5 and r/R=0.9 (where R is the tube radius) from left to right. The top row shows results for the 10.1 mm diameter tube. At the centreline of the jet (r/R=0) a perfectly monomodal distribution of droplet diameter is observed. Also, at r/R=0.5 the distribution is also monomodal, however a strongly bi-modal distribution is found near the jet wall, at r/R=0.9. The second row shows results for the 7.0 mm diameter tube clearly featuring a bi-modal distribution at both r/R=0.5 and r/R=0.9. Finally, the bottom row is for the 3.5 mm tube which also shows bimodality at r/R=0.5 and r/R=0.9. A feature for the 3.5 mm tube is that a very weak bimodality is also obtained on the jet centreline. These results are consistent with the concept of a liquid boundary layer developing on the inner walls leading to droplet shedding. The thickness of this layer depends on the length of the pipe but not its diameter so when the diameter narrows the boundary layer can extend to the pipe's centreline. The concept of droplet shedding is further confirmed in the high-speed imaging presented next.

Figure 5 shows representative Mie scattering images of the spray at the exit plane of the jet for several tube lengths. For the longer tube of 196 mm, the occurrence of strings of droplet filaments shed from the inner wall of the jet as shown in Fig. 5 is frequent. These filaments of droplets were found to have a relatively low velocity and are almost certainly the cause of the lower velocity leg in the bimodal scatter plots shown in Figs. 3 and 4.The frequency of the droplet shedding was found to decrease with tube length as is evident from the images shown for the 96 mm and 36 mm long tubes with the shortest tube of 6 mm showing no droplet shedding. It was estimated through observation of a large number of images that the frequency of shedding for the 196 mm tube was ~10% and this decreases to zero for the 6 mm tube. These findings provide an interpretation of the bimodality reported in Figs. 3-4 which in turn explains the reasons for the higher rms of fluctuations in the axial velocity measured for large droplets near the inner walls at the exit plane of these spray jets.

Conclusions

The spatial structure of reaction zones is reported here in a range of diluted sprays of acetone and ethanol fuels. The effects of increasing the spray loading or the jet velocity of the carrier are examined. It is found that in acetone flames and at low spray loading the reaction zones are broad and appear to be largely premixed. Increasing the liquid fuel loading for the same carrier velocity promotes a diffusion flame structure with thin outer reaction zones clearly separated from the central spray core while increasing the carrier velocity supports premixing and a return to broad reaction zones. In ethanol flames, the trends are different due to the different evaporation rate of the fuel. Increasing the spray loading leads to the formation of double reaction zones with the inner zones indicating significant premixing close to the jet

centreline. This double reaction zone structure gradually merges into one as the air carrier velocity increases.

The anomaly of the high rms of fluctuations measured for large droplets at the jet exit plane and near the inner wall of the pipe is explained as follows: For sufficiently long pipes, a liquid boundary layer develops on the inner wall and filaments from this layer are intermittently shed at the exit plane. These fragment into large, slow droplets and lead to the bimodal distribution of axial velocity measured at these locations and hence the high rms fluctuations.

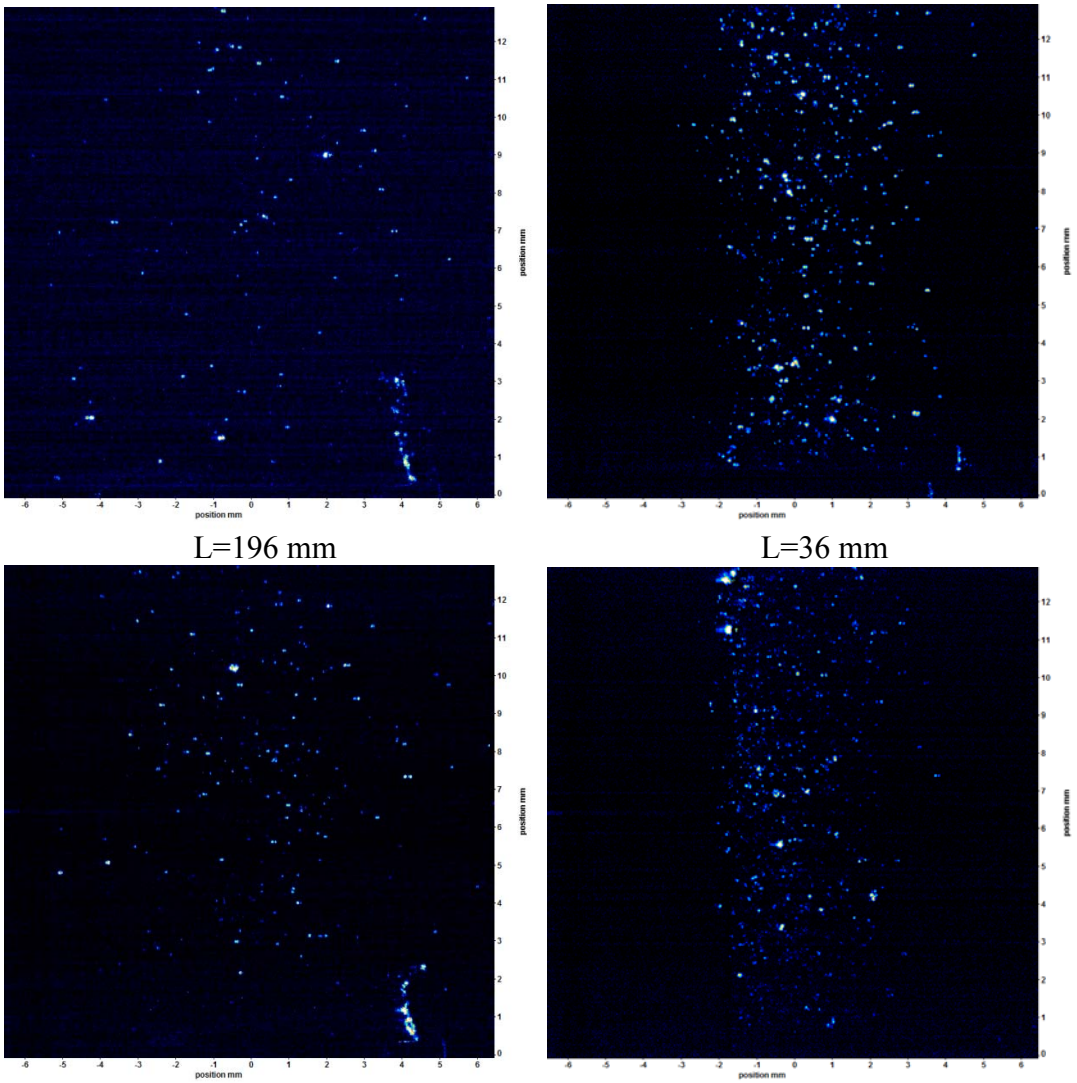

Figure 5: High speed images showing droplet Mie Scattering at the jet exit plane for different tube lengths of 10.1mm diameter. Note the droplet shedding for the 196 mm and 96mm tubes.

Acknowledgment
This research is supported by the Australian Research Council.

References

[1] Abani, N.,Reitz, R., *Diesel emgine emissions and combustion predictions using advanced mixing models applicable to fuel sprays.* Combust. Theory Modelling, 2010. **14**: p. 715-746.
[2] Bachalo, W.D., *Injection, dispersion, and combustion of liquid fuels*, in *Proc. Combust. Inst.* 1994, The Combustion Institute.: California. p. 333-344.

[3] Bazile, R.,Stepowski, D., *Measurements of vaporized and liquid fuel concentration fields in a burning spray jet of acetone using planar laser induced fluorescence.* Experiments in Fluids, 1995. **20**(1): p. 1-9.
[4] Bossard, J.A.,Peck, R.E., *Droplet size distribution effects in spray combustion*, in *Proc. Combust. Inst.* 1996, The Combustion Institute: Napoli. p. 1671-1677.
[5] DePaola, G., Mastorakos, E., Wright, Y.M.,Boulouchos, K., *Diesel engine simulations with multi-dimensional conditional moment closure.* Combust. Sci. Technol., 2008. **180**: p. 833-899.
[6] Faeth, G.M., *Spray combustion phenomena*, in *Proc. Combust. Inst.* 1996, The Combustion Institute: Napoli. p. 1593-1612.
[7] Faeth, G.M., Hsiang, L.P.,Wu, P.K., *Structure and breakup properties of sprays.* Int. J. Multiphase Flow, 1995. **21**: p. 99–127.
[8] Jiang, X., Siamas, G.A., Jagus, K.,T.G., K., *Physical modelling and advanced simulations of gas liquid two-phase jet flows in atomization and sprays.* Prog. Energy Combust. Sci., 2010. **36**: p. 131-167.
[9] Nijdam, J., Stårner, S.,Langrish, T., *An experimental investigation of droplet evaporation and coalescence in a simple jet flow.* Experiments in Fluids, 2004. **37**(4): p. 504-517.
[10] Raffaele Ragucci, Alessandro Bellofiore,Cavaliere, A., *Breakup and breakdown of bent kerosene jets in gas turbine conditions*, in *Proc. Combust. Inst.* 2007, The Combustion Institute. p. 2231-2238.
[11] Sornek, R.J., Dobashi, R.,Hirano, T., *Effects of turbulence on dispersion and vaporization of droplets in spray combustion*, in *Proc. Combust. Inst.* 2000, The Combustion Institute: Scotland. p. 1055-1062.
[12] Beck, C.H., Koch, R.,Bauer, H.J., *Identification of droplet burning modes in lean, partially prevaporized swirl-stabilized spray flames*, in *Proc. Combust. Inst.* 2009, The Combustion Institute. p. 2195-2203.
[13] Chen, G.,Gomez, A., *Dilute laminar spray diffusion flames near the transition from group combustion to individual droplet burning.* Combust. Flame, 1997. **110**(3): p. 392-404.
[14] Chen, Y.-C., Starner, S.H.,Masri, A.R., *A detailed experimental investigation of well-defined, turbulent evaporating spray jets of acetone.* Int. J. Multiphase Flow., 2006. **32**(4): p. 389-412.
[15] Masri, A.R.,Gounder, J.D., *Turbulent Spray Flames of Acetone and Ethanol Approaching Extinction.* Combustion Science and Technology, 2010. **182**(4): p. 702 - 715.
[16] Nakabe, K., Mizutani, Y., Hirao, T.,Fujioka, H., *An experimental study on detailed flame structure of liquid fuel sprays with and without gaseous fuel.* Combust. Flame, 1991. **84**(1-2): p. 3-14.
[17] Akamatsu, F., Mizutani, Y., Katsuki, M., Tsushima, S., Cho, Y.D.,Nakabe, K., *Group combustion behavior of droplets in a premixed-spray flame.* Atomization and Sprays, 1997. **7**(2): p. 199-218.
[18] Akamatsu, F., Mizutani, Y., Matsuki, M., Tsushima, S.,Cho, Y.D., *Group combustion behavior of premixed spray streams and group combustion number.* Nippon Kikai Gakkai Ronbunshu, B-hen, 1996. **62**(596): p. 1622-1628.
[19] Chiu, H.H., Kim, H.Y.,Croke, E.J., *Internal group combustion of liquid droplets*, in *Proc. Combust. Inst.* 1982, The Combustion Institute: Haifa. p. 971-980.
[20] Chiu, H.H.,Liu, T.M., *Group combustion of liquid droplets.* Combust. Sci. Technol., 1977. **17**(3-4): p. 127-42.
[21] *The International Workshop on Measurement and Computation of Turbulent Nonpremixed Flames,*. Available from: http://www.sandia.gov/TNF/abstracts.html.
[22] Masri, A.R., Dibble, R.W.,Barlow, R.S., *The Structure of Turbulent Nonpremixed Flames Revealed by Raman-Rayleigh-LIF Measurements.* Prog. Energy Combust. Sci., 1996. **22**(4): p. 307-362.
[23] Gounder, J.D.,Masri, A.R. *Flow Field and Mass Flux Measurements Near the Exit Plane of Spray Jets*. in *11th Triennial International Annual Conference on Liquid Atomization and Spray Systems*. 2009. Vail, Colorado, USA.
[24] Masri, A.R.,Gounder, J.D., *Details and Complexities of Boundary Conditions in Turbulent Piloted Dilute Spray Jets and Flames*, in *ERCOFTEC Chapter (details to be completed)*. 2011.